Optimization of intravascular shear stress assessment *in vivo*

Lisong Ai [a], Hongyu Yu [a], Wakako Takabe [a], Anna Paraboschi [a], Fei Yu [a], E.S. Kim [b],
Rongsong Li [a], Tzung K. Hsiai [a,*]

[a] *Department of Biomedical Engineering and Cardiovascular Medicine, University of Southern California, Los Angeles, CA 90089-1111, United States*
[b] *Department of Electrical Engineering and Electrophysics, University of Southern California, Los Angeles, CA 90089-1111, United States*

ABSTRACT

The advent of microelectromechanical systems (MEMS) sensors has enabled real-time wall shear stress (WSS) measurements with high spatial and temporal resolution in a 3-D bifurcation model. To optimize intravascular shear stress assessment, we evaluated the feasibility of catheter/coaxial wire-based MEMS sensors in the abdominal aorta of the New Zealand white (NZW) rabbits. Theoretical and computational fluid dynamics (CFD) analyses were performed. Fluoroscope and angiogram provided the geometry of aorta, and the Doppler ultrasound system provided the pulsatile flow velocity for the boundary conditions. The physical parameters governing the shear stress assessment in NZW rabbits included (1) the position and distance from which the MEMS sensors were mounted to the terminal end of coaxial wire or the entrance length, (L_e), (2) diameter ratios of aorta to the coaxial wire ($D_{aorta}/D_{coaxial\ wire} = 1.5$–9.5), and (3) the range of Reynolds numbers (116–1550). At an aortic diameter of 2.4 mm and a maximum Reynolds number of 212 (a mean Reynolds number of 64.2), the time-averaged shear stress (τ_{ave}) was computed to be 10.06 dyn cm^{-2} with a systolic peak at 33.18 dyn cm^{-2}. In the presence of a coaxial wire ($D_{aorta}/D_{coaxial\ wire} = 6$ and $L_e = 1.18$ cm), the τ_{ave} value increased to 15.54 dyn cm^{-2} with a systolic peak at 51.25 dyn cm^{-2}. Real-time intravascular shear stress assessment by the MEMS sensor revealed an τ_{ave} value of 11.92 dyn cm^{-2} with a systolic peak at 47.04 dyn cm^{-2}. The difference between CFD and experimental τ_{ave} was 18.5%. These findings provided important insights into packaging the MEMS sensors to optimize *in vivo* shear stress assessment.

© 2009 Elsevier Ltd. All rights reserved.

1. Introduction

Hemodynamic forces, namely, fluid shear stress, regulate the biological activities of the vascular endothelial cells (EC) (Ku, 1997) and vessel wall remodeling in the resistant arteries and aorta (Chatzizisis et al., 2008; Volokh and Vorp, 2008). Sedentary lifestyle promotes atherogenic hemodynamics in arterial bifurcations where oscillatory and low shear stress predisposes the development of atherosclerosis (Chatzizisis et al., 2007). The advent of microelectromecahnical systems (MEMS) provides an entry point to characterize the spatial and temporal variations of the WSS in various arterial configurations (Hsiai et al., 2004; Lasheras, 2007; Rouhanizadeh et al., 2005; Rouhanizadeh et al., 2006; Roy et al., 2006). Previously, silicon nitride was applied as an insulating layer on the diaphragm to enhance unidirectional heat transfer (Xu et al., 2005). In the new generation of MEMS sensors, biocompatible parylene C coating not only insulated the microelectronics but also provided flexibility for packaging the sensors to the catheter/coaxial wire.

Numerous computational fluid dynamics (CFD) codes have been developed to assess WSS with relevance to cardiovascular disease (Moore et al., 1998; Pedersen et al., 1997; Perktold et al., 1991). Steinman and Ethier investigated the effects of wall distensibility in a 2-D end-to-side anastomosis (Steinman and Ethier, 1994). Lei et al. (1997) further described the applications of CFD to design end-to-side anastomoses. Taylor et al. developed a stabilized FEM to simulate blood flow in the abdominal aorta under resting and exercise-induced pulsatile flow conditions (Taylor et al., 1998a, b, 1999). Hence, CFD codes predicted arterial regions where elevated temporal oscillations in shear stress are prone to vascular oxidative stress and inflammatory responses (Ai et al., 2008)

Despite numerous CFD solutions for WSS, there has been a paucity of experimental data. Conventionally, shear stress has been assessed by the direct and indirect methods (Schmidt et al., 1988). The former is based on both piezoresistive (Shajii et al., 1992) and capacitive readout schemes in a floating element sensing (Schmidt et al., 1988). The latter is based on convective heat transfer by correlating convective cooling of a heated element to shear stress. Indirect methods also include ultrasonic Doppler and magnetic resonance imaging (MRI). Both methods require a known geometry to correlate flow rates with shear

---

stress. While ultrasonic Doppler and MRI are non-invasive, the spatial resolution near the wall is difficult to establish.

To assess shear stress in the complicated arterial geometry, we developed the polymer-based sensors that are flexible, biocompatible, and deployable into the arterial system. The titanium (Ti) and platinum (Pt) layer embedded in the flexible polymer was used as the sensing elements. Based on heat-transfer principle (Yu et al., 2008), shear stress can be inferred from the heat loss from the heated sensing element to the flow in terms of the measured changes in voltage. The sensor was fabricated via surface micromachining technique utilizing parylene C as electrical insulation layer. The resistance of the sensing element was measured at approximately $1.0\,k\Omega$ and the signal-to-noise ratio was 4.8 (Yu et al., 2008). Direct measurement of wall shear stress in the aorta, thereby, enables us to predict the arterial regions exposed to low or oscillatory shear stress that is linked with the development of plaque formation.

To optimize intravascular shear stress (ISS) assessment, we performed both theoretical and CFD analyses. These analyses predicted the extent to which experimental parameters governed the deployment of the catheter/coaxial wire-based MEMS sensors into the aorta of NZW rabbits; namely, the diameter ratios of the aorta to the coaxial wires, position of sensors, and entrance length (L_e) in relation to the Reynolds number (Re).

2. Methods

2.1. Packaging and deployment of MEMS thermal sensors

We have developed biocompatible and flexible intravascular MEMS sensors to assess real-time ISS (Fig. 1a and b). The detailed operational principle and fabrication process of the MEMS sensor were previously described (Yu et al., 2008). The diameter of the coaxial wire was 0.4 mm and the length of the sensor was 4 cm (Fig. 1b). The biocompatible epoxy (EPO-TEK 301: Epoxy Technology, Billerica, MA, USA) was used to anchor the sensor to the coaxial wire (Fig. 1c). The sensor was packaged to the coaxial wire, which was deployed into the abdominal aorta of adult NZW rabbits under fluoroscopic guidance.

The sensors were first tested in the tube model and the shear stress measurements were validated by CFD simulation (Fig. 2a). A range of steady flow rates were generated by a flow system consisting of a digital modular drive (Master Flex L/S 77300-80, Cole-Palmer) and a pump drive (Master Flex L/S 7518-12, Cole-Palmer). The pump setting was calibrated using an electromagnetic flow meter (MAGFLO®, Danfoss A/S, DK). Once validated in the *in vitro* model, the MEMS sensors were deployed into the aorta of the rabbits through the coaxial wire via femoral cut-down procedure. Using the 3-D fluoroscopic guidance (Phillips BV-22HQ C-arm), the guide wire and MEMS sensors were visualized in the
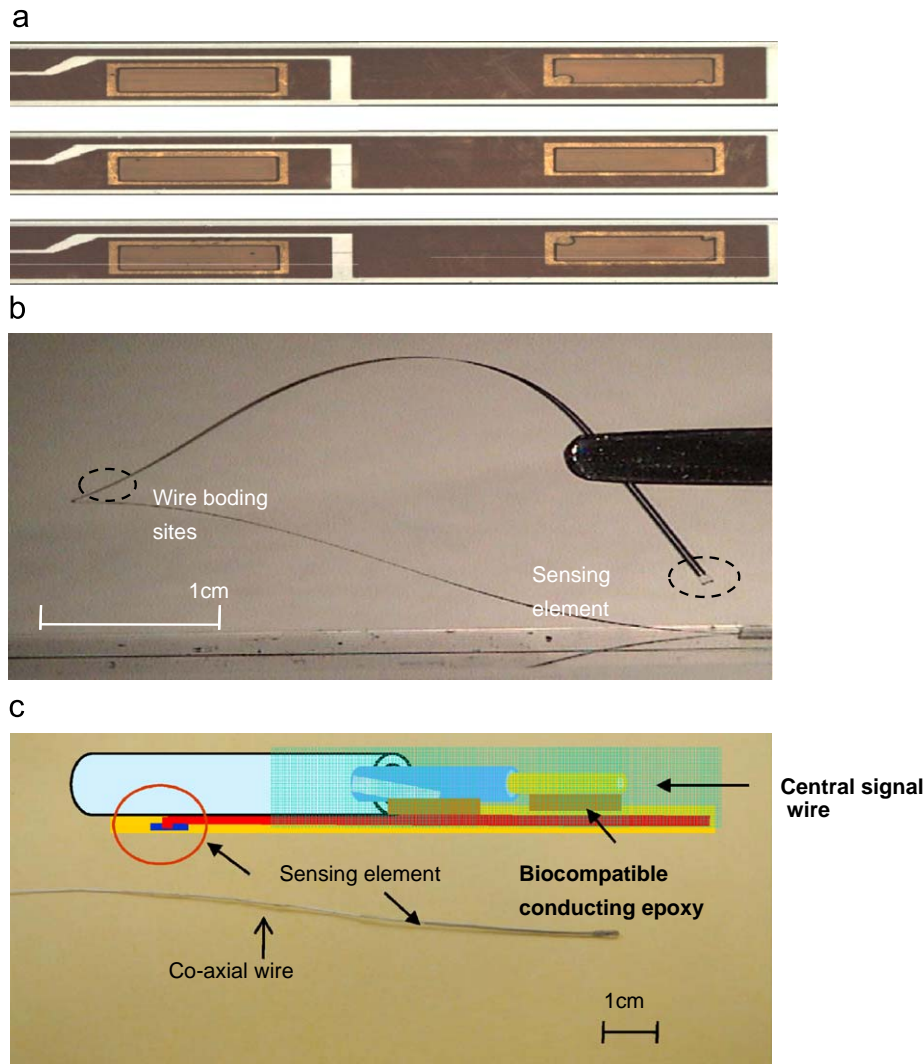

Fig. 1. Biocompatible and flexible intravascular sensors. (a) The sensor array on the wafer prior to release into individual devices. (b) The sensor could be bended or folded in a zigzag fashion without structural or functional damage. The Ti/Pt sensing element is located at the tip of the sensor. Located at the other end of the sensor are the wire-bonding sites for packaging to the terminal end of the electrical coaxial wire. (c) The biocompatible epoxy is used to anchor the sensor body onto the coaxial wire surface, and to insulate the electronic parts.
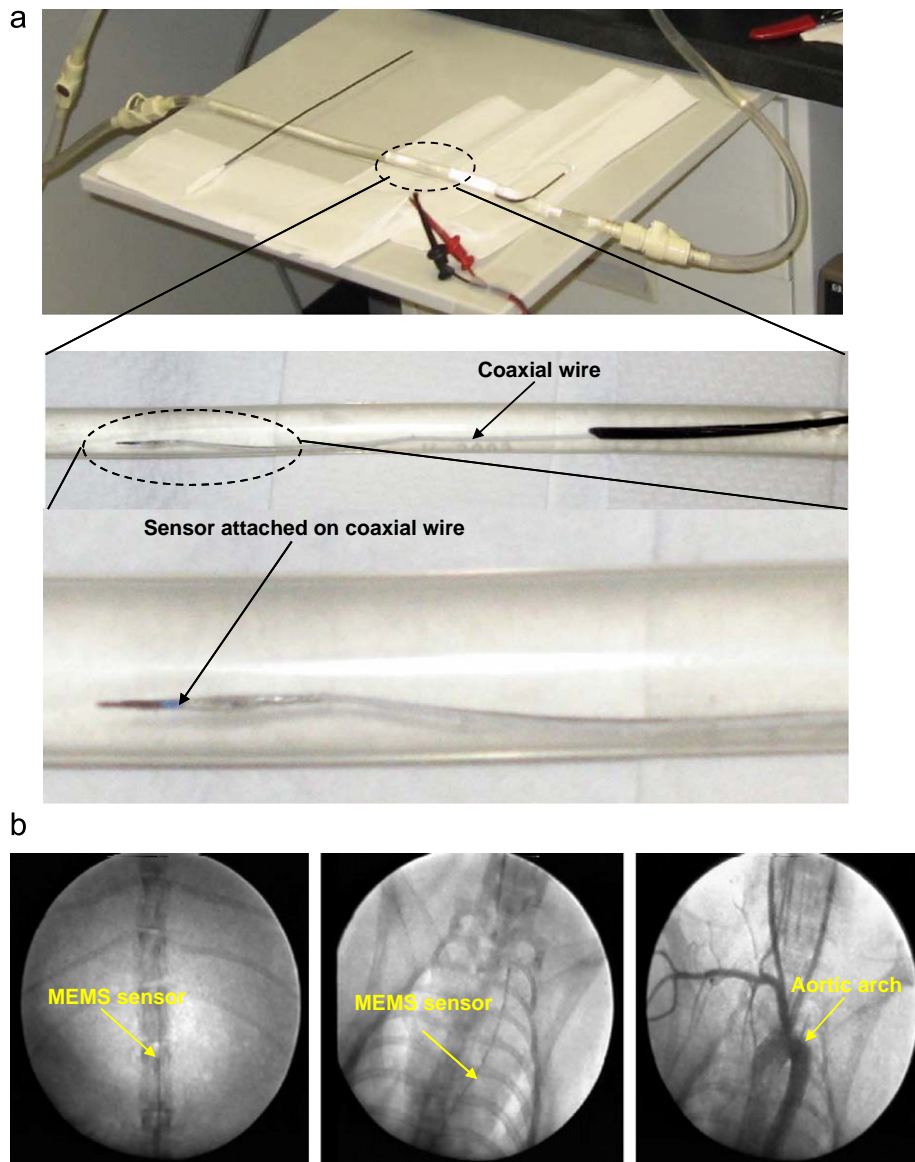
Fig. 2. The sensors were tested in a 3-D fluidic tube model. (a) The measurements were validated by CFD simulation with the geometry reconstructed from photos taken by a digital camera (b) Using fluoroscopic guidance in the animal angiographic lab, the operator was able to visualize and steer the sensor wire in the aorta of the NZW rabbits to the anatomic regions of interest; namely, the aortic arch and abdominal aorta. Contrast dye was injected to delineate the position of the wire in relation to the inner diameter of the aorta and the arterial branches.

abdominal aorta. The fluoroscope could be rotated to acquire the images in various planes. By injecting the contrast dye from the carotid artery, the operators were able to delineate the geometry of the rabbit aorta and the position of the coaxial wire in relation to the inner diameter of the aorta (Fig. 2b).

2.2. Theoretical and computational analyses of intravascular shear stress

2.2.1. Theoretical formulation to predict WSS in the presence of a catheter

Analogous to intravascular ultrasound (IVUS), the deployment of coaxial wires would inevitably influence the flow field (Back, 1994; Banerjee et al., 1999; Karahalios, 1990; Macdonald, 1982; Macdonald, 1986; Roy et al., 2006; Wentzel et al., 1997). To optimize the MEMS sensor measurement, we formulated Navier-Stokes equations analogous to flow in an annular duct to predict the flow disturbance when the catheter was positioned at the center (Fig. 3a). The viscosity, μ, was treated as a constant. The velocity profiles obtained for laminar flow in annulus and circular pipe were expressed as (Schetz and Fuhs, 1999)

$$U = -\frac{1}{4\mu}\frac{dP}{dx}\left[(R_i^2 - r^2) + \frac{n^2 - 1}{\ln n}R_i^2 \ln\frac{r}{R_i}\right] \quad (1)$$

$$u = -\frac{1}{4\mu}\frac{dp}{dx}R^2[1 - (r/R)^2] \quad (2)$$

where U and u represent the velocity in the annulus and circular pipe, respectively. R and R_i are the radii of the pipe and coaxial wire, respectively. n is the radius or diameter ratio between the vessel and the catheter, $n = R/R_i$, and dP/dx and dp/dx are the pressure gradient in the annulus and the circular pipe, respectively. The flow rate, Q, and WSS, τ_w, in the absence of coaxial wire were expressed as

$$Q = \int_0^R u2\pi r\,dr = -\frac{\pi}{8\mu}\frac{dp}{dx}R^4 \quad (3)$$

and

$$\tau_w = -\mu\frac{du}{dr}\Big|_{r=R} = -\frac{R}{2}\frac{dp}{dx} \quad (4)$$

2.2.2. Flow rates and wall shear stress

Assuming the effect of the coaxial wire on the flow was negligible (Doucette et al., 1992; Roy et al., 2005), the flow rate in the presence of coaxial wire would be defined as

$$Q = \int_{R_i}^R U2\pi r\,dr = -\frac{\pi}{8\mu}\frac{dP}{dx}R^4\frac{(n^4 - 1)\ln n - (n^2 - 1)^2}{n^4 \ln n} \quad (5)$$
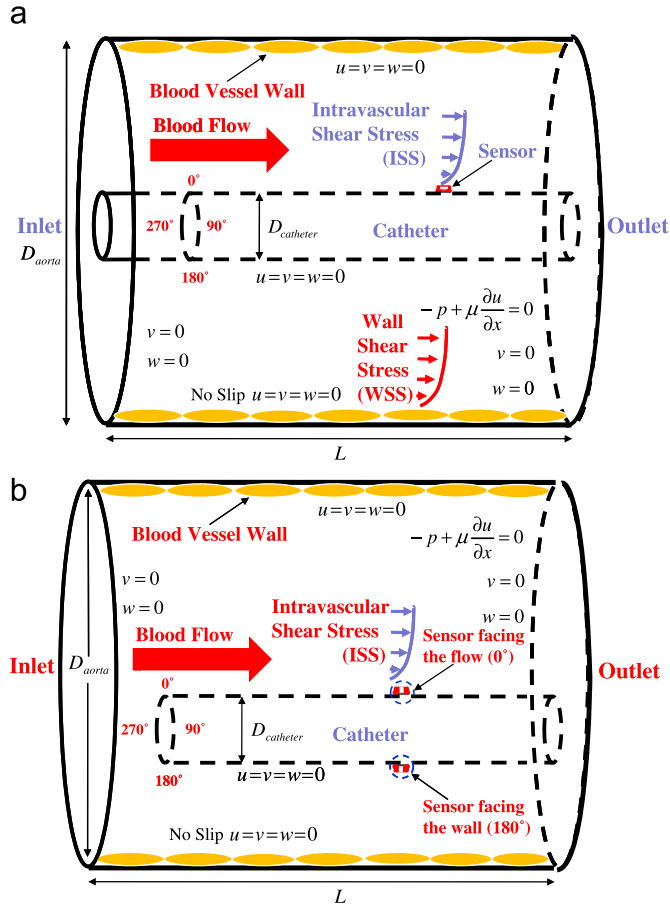
Fig. 3. The schematic diagram illustrates the geometry and boundary conditions for computational simulation. These conditions provided a basis to validate the *in vivo* intravascular shear stress (ISS) in relation to the WSS. The parameters, u, v and w, are the axial, radial and azimuthal velocity components, D_i represents the catheter diameter, and L is the vessel length. The red arrow indicates the flow direction. (a) The wire was assumed to be at the center and the flow disturbance caused by the wire tip was neglected during the theoretical study. (b) The effects of the wire tip and the wire positioning were analyzed in the computational study.

From Eq. (5), the following relation was obtained:

$$\frac{dP}{dx} = E_p \frac{dp}{dx} \tag{6}$$

where E_p is defined as the pressure elevation factor (PEF)

$$E_p = \frac{n^4 \ln n}{(n^4 - 1) \ln n - (n^2 - 1)^2} \tag{7}$$

From the velocity profile, U, the WSS in the presence of coaxial wire, τ_{w_wire}, was expressed as

$$\tau_{w\_wire} = -\mu \frac{du^*}{dr}\bigg|_{r=R} = E_{wss} \tau_w \tag{8}$$

where E_{wss} is the WSS elevation factor (WEF)

$$E_{wss} = \frac{n^2(2n^2 \ln n - n^2 + 1)}{2[(n^4 - 1) \ln n - (n^2 - 1)^2]} \tag{9}$$

Similarly, the shear stress on the MEMS sensor, τ_{i_wire}, was evaluated at $r = R_i$

$$\tau_{i\_wire} = -\mu \frac{dU}{dr}\bigg|_{r=R_i} = E_{iss} \tau_w \tag{10}$$

where τ_w is the WSS in the absence of coaxial wire and E_{iss} is defined as the ISS elevation factor (IEF)

$$E_{iss} = \frac{n^3(2 \ln n - n^2 + 1)}{2[(n^4 - 1) \ln n - (n^2 - 1)^2]} \tag{11}$$

2.3. Computational analyses

CFD analyses were performed to investigate the effects of the flow disturbance and the entrance length on the coaxial wire required to mount the MEMS sensors. The governing equations were solved for laminar, incompressible, and non-Newtonian flow. In our CFD model, the shear rate-dependent dynamic viscosity was implemented for the shear-thinning behavior of the rabbit blood (Bird et al., 1977; Boger, 1987). The simulations were performed for the geometry as shown in Fig. 3b.

In general, entrance length, L_e, is the distance required from the terminal end of the coaxial wire to the point where fully developed flow develops. The definition of the L_e (Sparrow et al., 1964) was also based on the length required to achieve a local incremental pressure drop of ~98% of the fully developed region. In our study, shear stress was used to predict L_e. The flow disturbance in the L_e region influenced heat transfer from the sensor to the flow stream (Liu et al., 1999). In this context, predicting the entrance length in relation to the Reynolds number guided the packaging of MEMS sensors to the coaxial wire.

The inlet Reynolds number, Re, was defined by the mean velocity

$$Re = \frac{\rho U_{mean} D}{\mu} \tag{12}$$

where U_{mean} is the mean flow velocity at the inlet.

2.3.1. Generation of 3-D geometries and meshes

The geometries of the tube model and the rabbit abdominal aorta model in the presence of coaxial wire or catheter were reconstructed in Pro-Engineer Wildfire V.3.0 (Parametric Technology, Needham, MA) using boundary conditions from experimental measurements. The models were imported into GAMBIT for mesh generation (Fluent Inc., Gambit 2.3.16, Lebanon, NH, USA). The meshed models were imported into the main CFD solver (Fluent Inc., Fluent 6.2.16, Lebanon, NH, USA) for further flow simulation. The CFD model was constructed with 78,868 cells, which were primarily the Tet/Hybrid elements. Since our focus was on the shear stress on the sensor, fine elements immediately adjacent to the coaxial wire were constructed to obtain sufficient information to characterize the large fluid velocity gradients near the wall.

In the abdominal aorta model, the flow field was solved under three catheter positioning schemes as described previously (Ai et al., 2008, 2009). The vessel inner diameter, D_{aorta}, was measured to be 2.4 mm from the angiogram (Fig. 3). The MEMS sensor was located 4.0 cm from the terminal end of the catheter/coaxial wire. Three different diameters ($D_{catheter}$) namely, 0.25 mm (mouse catheter 0.010 mm in OD), 0.4 mm (coaxial wire), and 0.97 mm (dog catheter 0.038 in OD), were studied in the CFD simulations. The geometry of the computational model of rabbit abdominal aorta is shown in Fig. 3b, where u and v represent the axial and radial velocities, and $D_{catheter}$ represents the catheter diameter.

2.3.2. Boundary conditions

The steady flow rates from the *in vitro* experiment were applied as the inlet flow boundary condition for the corresponding 3-D computational model. The ultrasound transducer (Philips SONOS 5500 at 12 MHz) was used to obtain the pulsatile velocity waveform. The recorded profile of the centerline velocity, U_c, as shown in Fig. 4a, was reconstructed by applying the Fourier analysis using 12 harmonics (Fig. 4b). The peak and time-averaged velocity were 57.7 and 14.6 cm s^{-1}, respectively. The period of one cardiac cycle, T, was 0.33 s corresponding to 180 beats min^{-1}. From Eq. (12), the mass flux at the inlet in the axial direction (n_x) was obtained as

$$n_x = \frac{\mu_\infty Re}{d} \tag{13}$$

The calculated mass flux was applied as the inlet boundary condition and implemented by a user defined C++ code in FLUENT.

The traction-free condition was assumed at flow outlet. No-slip boundary condition was applied to the inner walls and the surface of the coaxial wire.

The spatial WSS, τ_w, was calculated for incompressible fluids as

$$\tau_w = -\mu \frac{\partial u_t}{\partial n}\bigg|_{wall} \tag{14}$$

where u_t is the velocity tangential to the wall and n is the unit vector perpendicular to the wall.

A range of steady flow rates were also studied to establish the relationship between the entrance length and flow rate. The mean flow velocity was maintained at 0.158, 0.288, 0.625, 0.92654, and 1.567 m s^{-1}, yielding Reynolds numbers of 116, 210, 330, 439, 680, 910, 1150, 1350, and 1550. The Reynolds numbers of 116 and 439 represented the time-averaged value and the maximum value in the rabbit thoracic aorta, respectively. Comparatively, the Reynolds number of 1150 represented the maximal value in the human descending aorta.

Reynolds numbers were determined in the presence or absence of coaxial wire. The hydraulic diameter, $D_h = D - D_i$, was used to normalize the Reynolds number
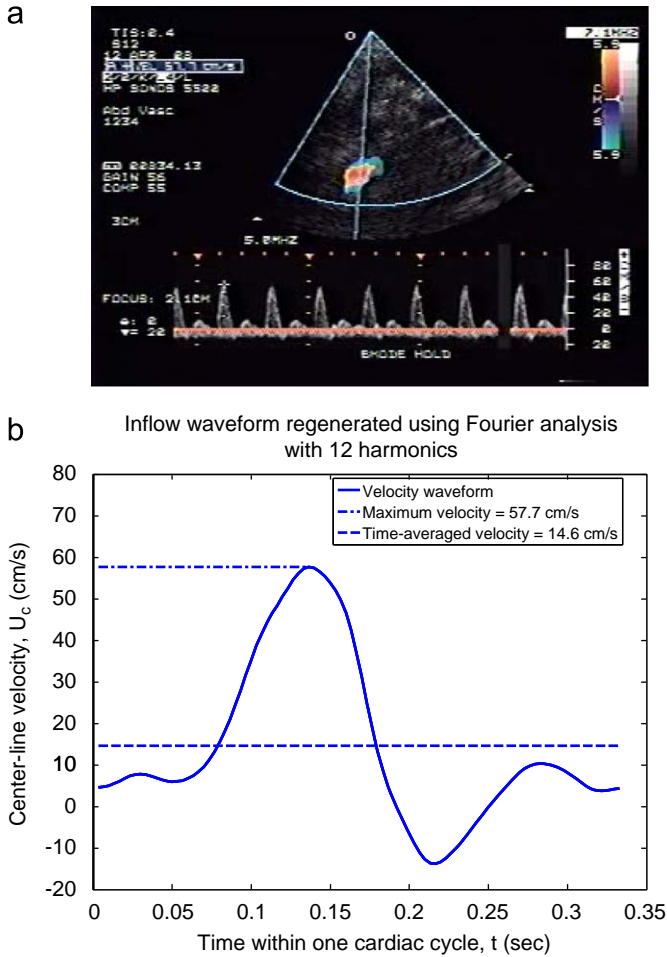
a

b

Inflow waveform regenerated using Fourier analysis with 12 harmonics

Fig. 4. The pulsatile velocity waveform was derived from Doppler ultrasound measurement and reconstructed using Fourier analysis with 12 harmonics for computational simulation. (a) The centerline velocity profile, including the peak velocity, was recorded. (b) The recorded velocity profile was reconstructed with 12 harmonics by applying Fourier analysis.

and the entrance length, L_e. In the absence of a catheter, the Reynolds number was expressed in terms of the flow rate, Q

$$Re = \frac{\rho U_{mean} D}{\mu} = \frac{4\rho Q}{\mu \pi D} \tag{15}$$

Given that in the presence of catheter,

$$Q = U_{mean\_wire} \times area = U_{mean\_wire} \pi (D^2 - D_i^2)/4 \tag{16}$$

the Reynolds number, Re_{wire}, was calculated from the mean velocity U_{mean_wire}

$$Re_{wire} = \frac{\rho U_{mean\_wire} D_h}{\mu} = \frac{4\rho Q}{\mu \pi (D + D_i)} \tag{17}$$

We assumed the effect of the catheter on the flow to be negligible (Doucette et al., 1992; Roy et al., 2005)

$$Re_{wire} = Re \frac{D}{D + D_i} \tag{18}$$

$$L_{e\_wire} = L_e/D_h \tag{19}$$

The normalized entrance length, L_{e_wire} as a function of the normalized Reynolds number, Re_{wire}, was derived using the curve fitting toolbox of MATLAB 7.1 (Math-works, Natick, USA).

3. Results

3.1. Theoretical prediction of WSS in the presence of a coaxial wire

The diameter ratio influenced the extent to which the coaxial wire increased the pressure and WSS measurements in a 3-D tube. This change in velocity profile reversed the direction of shear stress, leading to an increase in shear stress on the coaxial wire by an elevation factor (E_{iss}). Fig. 5a illustrated an increase in pressure by an elevation factor (E_p) as a function of the diameter ratio. The magnitude of E_p decreased significantly from 24.2 to 2.5 as the ratio increased from 1.5 to 4.5 with an asymptotic value of 1.28 at a diameter ratio approaching 100. The pressure was predicted to increase by 20% at a diameter ratio of 100.
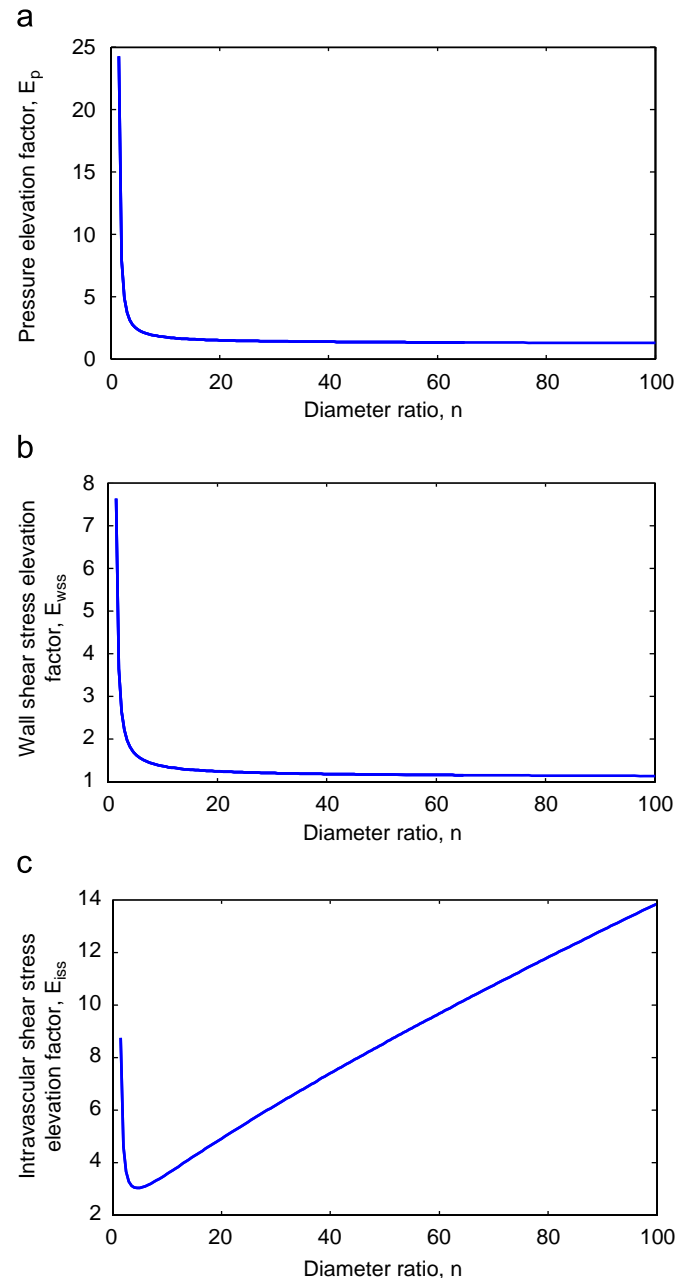
a

b

c

Fig. 5. Variations in elevation factors as a function of the diameter ratio, n. (a) Pressure elevation factor, E_p, as a function of n. (b) WSS elevation factor, E_{wss}, as a function of n. (c) ISS elevation factor, E_{iss}, as a function of n.

Wall shear stress and WSS elevation factor (E_{wss}) were also dependent on the diameter ratio (Fig. 5b). E_{wss} decreased from 7.6 to 1.7 as the diameter ratio increased from 1.5 to 4.5. The elevation factor for ISS on the coaxial wire (E_{iss}) was reduced from 8.747 to its minimum of 3.024 as the diameter ratio increased from 2 to 4.5 (Fig. 5c). In humans, the large diameter ratio would minimize the WSS elevation to ~10%. Taken together, a large catheter ($n < 2$) would introduce significant elevations in pressure and shear stress, whereas $n > 4.5$ would minimize these effects (Anderson et al., 1986).

3.2. Shear stress assessment in a 3-D tube model

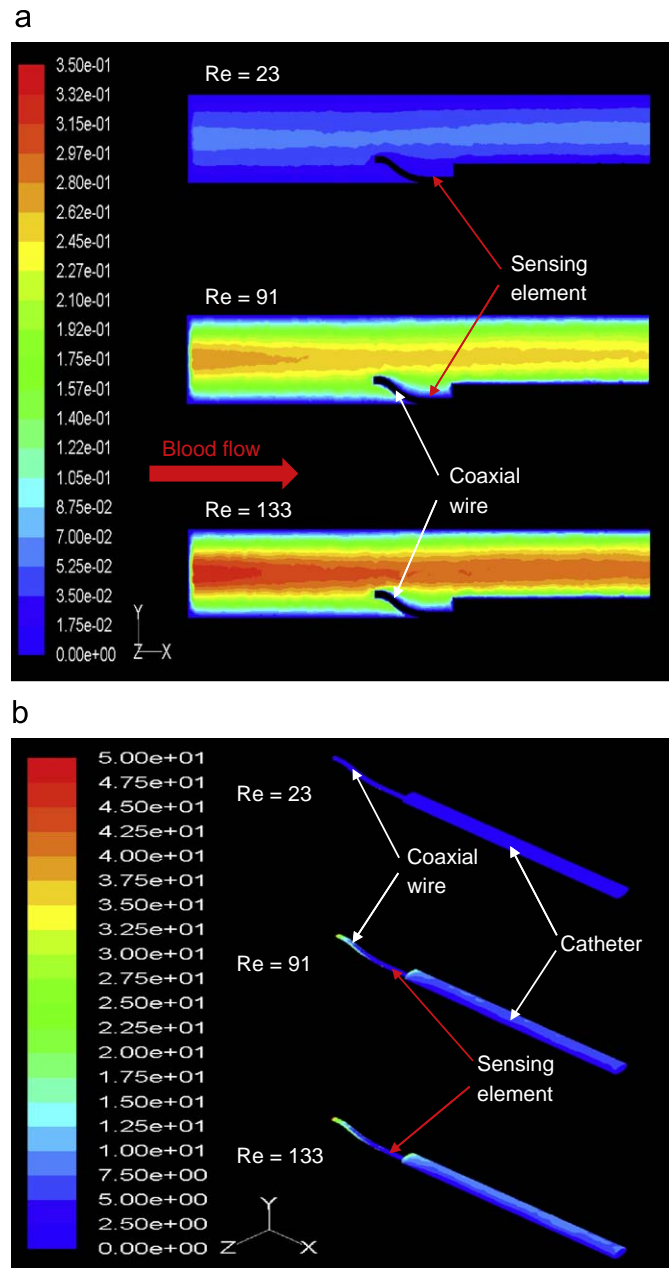CFD simulation was performed to analyze both velocity profiles and shear stress distribution on the catheter/coaxial wire in response to three distinct Reynolds numbers; namely, 23, 91, and 133 (Fig. 6). The effects of flow disturbance on the MEMS sensors were negligible in the presence of a coaxial wire until the Reynolds number reached above 133 (Fig. 6a and b). At a Reynolds number of 23, shear stress on the coaxial wire was 0.59 dyn cm^{-2}; at a Reynolds number of 91, shear stress was 3.13 dyn cm^{-2}; and at 133, shear stress was 5.61 dyn cm^{-2}. Next, real-time shear stress assessment by the MEMS sensor was compared with that of CFD solutions (Fig. 7). The relationship between the voltage changes and flow rates (Fig. 7a) were converted to shear stress using the calibration curve (Fig. 7b) (Yu et al., 2008). Real-time shear stress measurement was in good agreement with that of CFD at flow rates greater than 6 ml s^{-1}.

3.3. Entrance length and Reynolds numbers

The normalized entrance length, L_{e_wire}, and its corresponding normalized Reynolds number, Re_{wire}, were determined based on the CFD results (Fig. 8). A relation between Re_{wire} and L_{e_wire} derived from CFD was expressed as

$$L_{e\_wire} = 0.008184 Re_{wire} \qquad (20)$$

Fig. 6. CFD simulation was performed at various flow rates to analyze both velocity profiles and shear stress distributions on the coaxial wire. (a) The velocity profiles in response to three distinct flow rates ($Re = 23$, 91, and 133, respectively). (b) The shear stress distributions on the coaxial wire and catheter in response to the three flow rates in Fig. 6a.
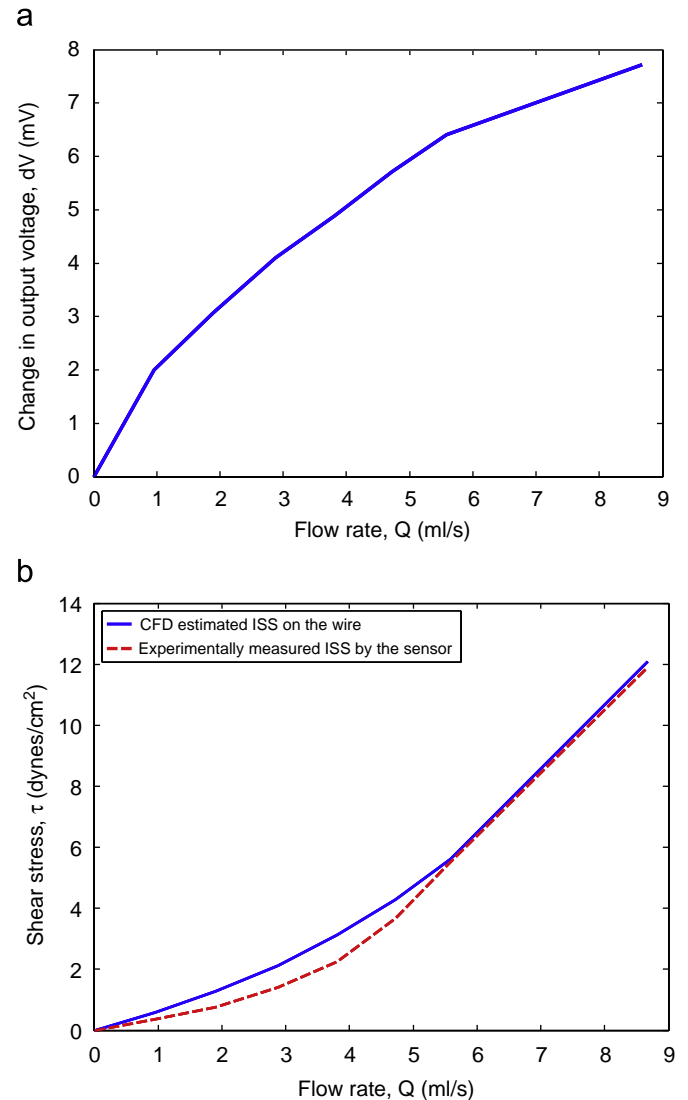

Fig. 7. The experimental ISS as detected by the MEMS sensor was compared with the computational solutions. (a) The relationship between the voltage changes and flow rates. (b) The converted shear stress using our previously reported calibration curve was compared with the computational solutions.
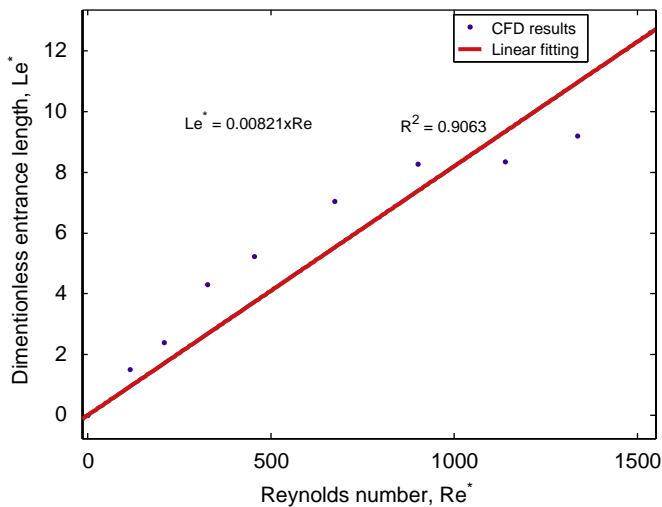
Fig. 8. The normalized entrance length, L_e^*, and its corresponding normalized Reynolds number, Re^*, were determined based on the CFD results.

L_{e_wire} increased in a relatively linear fashion as a function of Re_{wire}. This relation enabled us to mount the MEMS sensors downstream from the terminal end of coaxial wire to optimize real-time shear stress assessment.

3.4. Shear stress assessment in the abdominal aorta of NZW rabbits

The entrance lengths were determined as a function of flow rates by the computational results. The MEMS sensor was positioned at 4 cm from the terminal end of the coaxial wire. The inflow boundary conditions obtained from the Doppler ultrasound were incorporated into the CFD simulations.

The position of the coaxial wire and the orientation of the sensors facing the flow field significantly influenced ISS assessment. At the diameter ratio of 6, L_e of 1.18 cm, and position of the coaxial wire at the center, the time-averaged shear stress (τ_{ave}) on the coaxial wire was computed to be 31.2 dyn cm^{-2} with a systolic peak at 102.8 dyn cm^{-2} (corresponding to a maximum Reynolds number of 212). Despite the identical afore-mentioned physical parameters, a shift in the coaxial position at 0.2 mm off the center resulted in an asymmetric distribution of shear stress on the coaxial wire from $\tau_{0°} = 97.8$ dyn cm^{-2} at 0°, $\tau_{90°} = 107.6$ dyn cm^{-2} at 90°, to $\tau_{180°} = 112.8$ dyn cm^{-2} at 180° corresponding to a maximum Reynolds number of 212. Similarly, positioning the coaxial wire at 0.1 mm away from the vessel wall, the shear stress at the peak of systole was $\tau_{0°} = 6.9$ dyn cm^{-2} at 0°, $\tau_{90°} = 53.6$ dyn cm^{-2} at 90°, and $\tau_{180°} = 98.3$ dyn cm^{-2} at 180°.

CFD analysis revealed that the presence of a coaxial wire ($D_{aorta}/D_{coaxial\ wire} = 6$ and $L_e = 1.18$ cm) increased the time-averaged WSS (τ_{ave}) from 10.06 to 15.5 dyn cm^{-2} and the systolic peak from 33.2 to 51.3 dyn cm^{-2} (Fig. 9). Experimentally, under fluoroscopic visualization, real-time ISS assessment by the coaxial wire near the wall with the MEMS sensor facing the flow field revealed τ_{ave} value of 11.92 dyn cm^{-2} with a systolic peak at 47.04 dyn cm^{-2}. The difference between CFD and experimental τ_{ave} was 18.5%. Taken together, our findings demonstrated that deploying the coaxial wire using a steerable catheter under 3-D fluoroscopic guidance along with the angiogram would optimize real-time shear stress assessment.
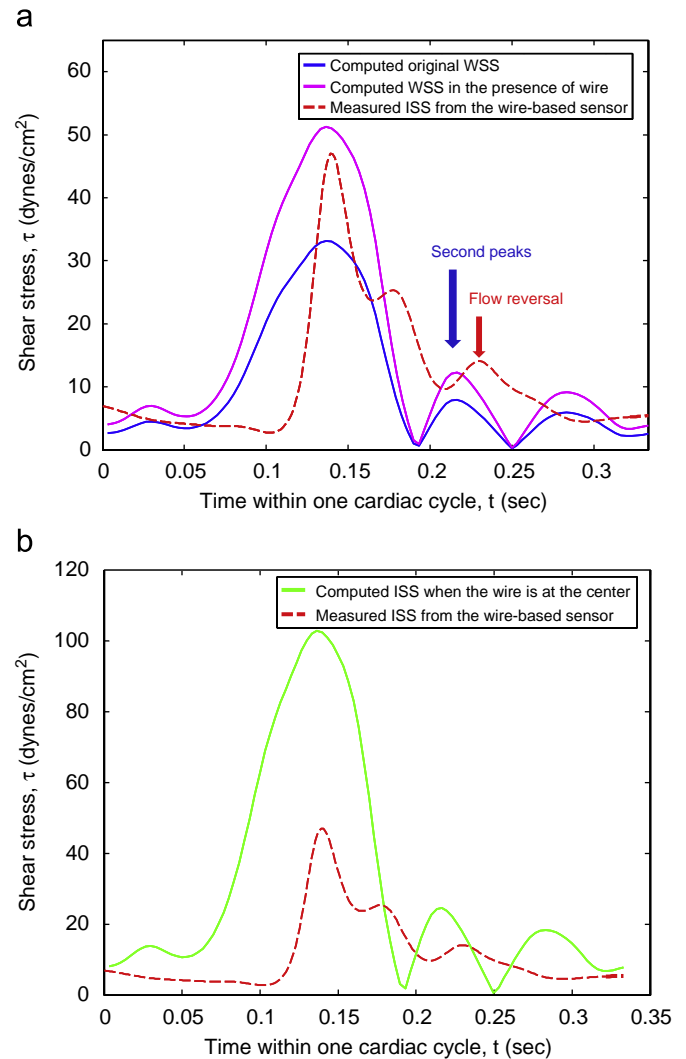

Fig. 9. Measured shear stress tracing in one cardiac cycle was compared with CFD solutions. (a) Superimposed on the real-time ISS profile (red dashed line) are the CFD solutions of WSS before (blue) and after (magenta) the coaxial wire was positioned at the center. The waveform of the ISS measurement overlapped with those of the computed ones despite the differences in magnitude. (b) Comparison between the real-time ISS profile (red dashed line) and computed ISS values on the coaxial wire positioned at the center. (For interpretation of the references to colour in this figure legend, the reader is referred to the web version of this article.)

4. Discussion

In this study, we performed theoretical and CFD analyses to optimize real-time intravascular assessment in the aorta of NZW rabbits. CFD analyses revealed that an entrance length of 2.9 mm and the diameter ratio ($n = 4.5$) would minimize the pressure and shear stress elevation in the rabbit aorta. When the catheter was positioned off the center of vessel, Velusamy and Garg (1994) reported that an eccentricity of the velocity profiles developed, and shear stress on the catheter and the vessel wall varied circumferentially (Ai et al., 2008, 2009) (Fig. 3b). In humans, the diameter ratio could approach to 100 for an aortic inner diameter of 2.5 cm with a catheter outer diameter of 0.254 mm. Hence, ISS assessment could be further optimized by positioning the catheter near the vessel wall using a steerable catheter with a large diameter ratio, such as a large animal model.

Several equations for estimating entrance length had been proposed (Shah, 1978; Wojtkowiak and Popiel, 2006). Among

these was the one proposed by Wojtkowiak and Popiel (2006) for flow in an annular duct. The slope of their linear equation, 0.0161, was about twice as our estimation at 0.008184. One reason for this deviation was the criteria used to define the fully developed flow. We adopted the notion that the wall shear rate converges to its fully developed value at about half the length at which the centerline velocity converges to its fully developed value (Ku, 1997).

Despite numerous CFD solutions for wall shear stress, there has been a paucity of experimental data. A 30% distortion is commonly encountered for experimental intravascular measurements (Ku, 1997). The boundary conditions and dimensions implemented in the CFD model might not precisely reflect the experimental boundary conditions. Therefore, the center-positioning scheme and the CFD results provided a basis to compare with direct sensor measurement.

Our computational results indicated that the entrance length in response to the maximal inlet Reynolds numbers in the rabbits ($Re_{max\_rabbit} = 459$) and human abdominal aorta ($Re_{max\_human} = 1150$) were $L_{e\ rabbit} = 1.244$ cm and $L_{e\ human} = 1.985$ cm, respectively. For a Womersley number greater than 1, the above L_e values could be overestimated. Sufficient time was allowed for the flow to develop towards a parabolic velocity profile during individual cardiac cycles (Ai et al., 2008, 2009) and the pulsatile flow behaved in a quasi-steady manner (Fung, 1997). The MEMS sensing element were mounted at 4.0 cm downstream from the terminal end of the coaxial wire; thereby, optimizing intravascular measurements.

In conclusion, ISS assessment was validated in vitro by deploying the catheter-based MEMS sensors in a 3-D model. Theoretical and computational models further provided physical parameters to optimize real-time shear stress assessment. These fundamental analyses provided a basis to further investigate the application of MEMS devices (Rouhanizadeh et al., 2006) for in vivo studies.

Conflict of interest statement

I declare no conflict of interest

References

Ai, L., Rouhanizadeh, M., Wu, J.C., Takabe, W., Yu, H., Alavi, M., Li, R., Chu, Y., Miller, J., Heistad, D., Hsiai, T.K., 2008. Shear stress influences spatial variations in vascular Mn-SOD expression: implication for LDL nitration. American Journal of Physiology Cell Physiology, C1576–C1585.

Ai, L., Yu, H., Hale, S., Dai, W., Li, R., Kloner, R., Hsiai, T.K., 2009. Real-time Intravascular Shear Stress in the Rabbit Abdominal Aorta. IEEE Transactions on Biomedical Engineering, in press.

Anderson, H.V., Zaatari, G.S., Roubin, G.S., Leimgruber, P.P., Gruentzig, A.R., 1986. Steerable fiberoptic catheter delivery of laser energy in atherosclerotic rabbits. American Heart Journal 111, 1065–1072.

Back, L.H., 1994. Estimated mean flow resistance increase during coronary-artery catheterization. Journal of Biomechanics 27, 169–175.

Banerjee, R.K., Back, L.H., Back, M.R., Cho, Y.I., 1999. Catheter obstruction effect on pulsatile flow rate-pressure drop during coronary angioplasty. Journal of Biomechanical Engineering Transactions of the ASME 121, 281–289.

Bird, R.B., ARC, A., Hassager, O., 1977. Dynamics of Polymeric Liquids. Fluid Mechanics, Vol.1. Wiley, New York, 470pp.

Boger, D.V., 1987. Viscoelastic flows through contractions. Annual Review of Fluid Mechanics 19, 157–182.

Chatzizisis, Y.S., Coskun, A.U., Jonas, M., Edelman, E.R., Feldman, C.L., Stone, P.H., 2007. Role of endothelial shear stress in the natural history of coronary atherosclerosis and vascular remodeling-molecular, cellular, and vascular behavior. Journal of the American College of Cardiology 49, 2379–2393.

Chatzizisis, Y.S., Jonas, M., Coskun, A.U., Beigel, R., Stone, B.V., et al., 2008. Prediction of the localization of high-risk coronary atherosclerotic plaques on the basis of low endothelial shear stress—an intravascular ultrasound and histopathology natural history study. Circulation 117, 993–1002.

Doucette, J.W., Corl, P.D., Payne, H.M., Flynn, A.E., Goto, M., et al., 1992. Validation of a doppler guide wire for intravascular measurement of coronary-artery flow velocity. Circulation 85, 1899–1911.

Fung, Y.C., 1997. Biomechanics: Circulation. Springer, Berlin, 130–132 pp.

Hsiai, T.K., Cho, S.K., Wang, P.K., Ing, M.H., Salazar, A., et al., 2004. Micro sensors: linking vascular inflammatory responses with real-time oscillatory shear stress. Annals of Biomedical Engineering 32, 189–201.

Karahalios, G.T., 1990. Some possible effects of a catheter on the arterial-wall. Medical Physics 17, 922–925.

Ku, D.N., 1997. Blood flow in arteries. Annual Review of Fluid Mechanics 29, 399–434.

Lasheras, J.C., 2007. The biomechanics of arterial aneurysms. Annual Review of Fluid Mechanics 39, 293–319.

Lei, M., Archie, J.P., Kleinstreuer, C., 1997. Computational design of a bypass graft that minimizes wall shear stress gradients in the region of the distal anastomosis. Journal of Vascular Surgery 25, 637–646.

Liu, C., Huang, J.B., Zhu, Z.J., Jiang, F.K., Tung, S., et al., 1999. Micromachined flow shear stress sensor based on thermal transfer principles. Journal of Microelectromechanical Systems 8, 90–99.

Macdonald, D.A., 1982. Fully developed incompressible flow between non-coaxial circular-cylinders. Zeitschrift Fur Angewandte Mathematik Und Physik 33, 737–751.

Macdonald, D.A., 1986. Pulsatile flow in a catheterized artery. Journal of Biomechanics 19, 239–249.

Moore, J.A., Steinman, D.A., Ethier, C.R., 1998. Computational blood flow modelling: errors associated with reconstructing finite element models from magnetic resonance images. Journal of Biomechanics 31, 179–184.

Pedersen, E.M., Agerbaek, M., Kristensen, I.B., Yoganathan, A.P., 1997. Wall shear stress and early atherosclerotic lesions in the abdominal aorta in young adults. European Journal of Vascular and Endovascular Surgery 13, 443–451.

Perktold, K., Resch, M., Peter, R.O., 1991. 3-dimensional numerical-analysis of pulsatile flow and wall shear stress in the carotid-artery bifurcation. Journal of Biomechanics 24, 409–420.

Rouhanizadeh, M., Lin, T.C., Arcas, D., Hwang, J., Hsiai, T.H., 2005. Spatial variations in shear stress in a 3-D bifurcation model at low Reynolds numbers. Annals of Biomedical Engineering 33, 1360–1374.

Rouhanizadeh, M., Soundararajan, G., Ascara, D., Lo, R., Browand, F., Hsiai, T., 2006. MEMS sensors to resolve spatial variations in shear stress in a 3-D bifurcation model. IEEE Sensors 6, 78–88.

Roy, A.S., Banerjee, R.K., Back, L.H., Back, M.R., Khoury, S., Millard, R.W., 2005. Delineating the guide-wire flow obstruction effect in assessment of fractional flow reserve and coronary flow reserve measurements. American Journal of Physiology: Heart and Circulatory Physiology 289, H392–H397.

Roy, A.S., Back, L.H., Banerjee, R.K., 2006. Guide wire flow obstruction effect on pressure drop-flow relationship in moderate coronary artery stenosis. Journal of Biomechanics 39, 853–864.

Schetz, J.A., Fuhs, A.E. (Eds.), 1999. Fundamentals of Fluid Mechanics. Wiley, New York.

Schmidt, M.A., Howe, R.T., Senturia, S.D., Haritonidis, J.H., 1988. Design and calibration of a microfabricated floating-element shear stress sensor. IEEE Transactions on Electron Devices 35, 750–757.

Shah, R.K., 1978. Correlation for laminar hydrodynamic entry length solutions for circular and noncircular ducts. Journal of Fluids Engineering Transactions of the Asme 100, 177–179.

Shajii, J., Ng, K.Y., Schmidt, M.A., 1992. A microfabricated floating element shear stress sensor using wafer-bonding technology. Journal of Microelectromechanical Systems, 89–94.

Sparrow, E.M., Lin, S.H., Lundgren, T.S., 1964. Flow development in the hydrodynamic entrance region of tubes and ducts. Physics of Fluids 7, 338–347.

Steinman, D.A., Ethier, C.R., 1994. The effect of wall distensibility on flow in a 2-dimensional end-to-side anastomosis. Journal of Biomechanical Engineering Transactions of the Asme 116, 294–301.

Taylor, C.A., Hughes, T.J.R., Zarins, C.K., 1998a. Finite element modeling of blood flow in arteries. Computer Methods in Applied Mechanics and Engineering 158, 155–196.

Taylor, C.A., Hughes, T.J.R., Zarins, C.K., 1998b. Finite element modeling of three-dimensional pulsatile flow in the abdominal aorta: relevance to atherosclerosis. Annals of Biomedical Engineering 26, 975–987.

Taylor, C.A., Hughes, T.J.R., Zarins, C.K., 1999. Effect of exercise on hemodynamic conditions in the abdominal aorta. Journal of Vascular Surgery 29, 1077–1089.

Velusamy, K., Garg, V.K., 1994. Entrance flow in eccentric annular ducts. International Journal for Numerical Methods in Fluids 19, 493–512.

Volokh, K.Y., Vorp, D.A., 2008. A model of growth and rupture of abdominal aortic aneurysm. Journal of Biomechanics 41, 1015–1021.

Wentzel, J.J., Krams, R., van der Steen, A.F.W., Li, W., Cespedes, E.I., Bom, N., Slager, C.J., 1997. Disturbance of 3-D velocity profiles induced by IVUS catheter, evaluation with computational fluid dynamics. Computers in Cardiology IEEE, 597–599.

Wojtkowiak, J., Popiel, C.O., 2006. Inherently linear annular-duct-type laminar flowmeter. Journal of Fluids Engineering Transactions of the Asme 128, 196–198.

Xu, Y., Lin, Q., Lin, G.Y., Katragadda, R.B., Jiang, F.K., et al., 2005. Micromachined thermal shear stress sensor for underwater applications. Journal of Microelectromechanical Systems 14, 1023–1030.

Yu, H., Ai, L., Rouhanizadeh, M., Patel, D., Kim, E.S., Hsiai, T.K., 2008. Flexible polymer sensors for in vivo intravascular shear stress analysis. IEEE/ASME Journal Microelectromachanical Systems 17, 1178–1186.